JCTC Journal of Chemical Theory and Computation

pubs.acs.org/JCTC Article

Optimal Orbital Selection for Full Configuration Interaction (OptOrbFCI): Pursuing the Basis Set Limit under a Budget

Yingzhou Li* and Jianfeng Lu*

Cite This: *J. Chem. Theory Comput.* 2020, 16, 6207−6221

Read Online

ACCESS | Metrics & More | Article Recommendations

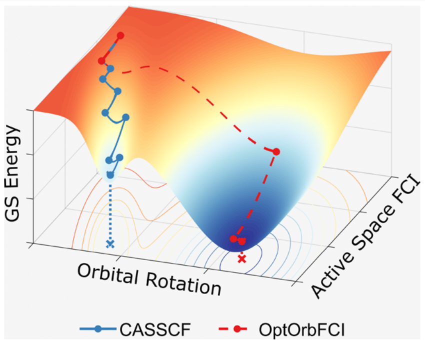

ABSTRACT: Full configuration interaction (FCI) solvers are limited to small basis sets due to their expensive computational costs. An optimal orbital selection for FCI (OptOrbFCI) is proposed to boost the power of existing FCI solvers to pursue the basis set limit under a computational budget. The optimization problem coincides with that of the complete active space SCF method (CASSCF), while OptOrbFCI is algorithmically quite different. OptOrbFCI effectively finds an optimal rotation matrix via solving a constrained optimization problem directly to compress the orbitals of large basis sets to one with a manageable size, conducts FCI calculations only on rotated orbital sets, and produces a variational ground-state energy and its wave function. Coupled with coordinate descent full configuration interaction (CDFCI), we demonstrate the efficiency and accuracy of the method on the carbon dimer and nitrogen dimer under basis sets up to cc-pV5Z. We also benchmark the binding curve of the nitrogen dimer under the cc-pVQZ basis set with 28 selected orbitals, which provide consistently lower ground-state energies than the FCI results under the cc-pVDZ basis set. The dissociation energy in this case is found to be of higher accuracy.

1. INTRODUCTION

Quantum many-body problems in electronic structure calculations remain difficult for strongly correlated (multireference) systems. Both the infamous sign problem and the combinatorial scaling make the problem intractable in a large basis set setting. In this paper, we propose an optimal orbital selection for FCI (OptOrbFCI) to solve full configuration interaction (FCI) problems on large basis sets under limited memory and computational power budget.

In the past decades, methods for solving FCI problems have been developed rapidly, which gives an acceleration of a factor of hundreds or even more compared with conventional methods. Among these efficient FCI solvers, the density matrix renormalization group (DMRG)[1,2] employs a matrix product state ansatz in representing the ground-state wave function and then finds variational solutions. Full configuration interaction quantum Monte Carlo (FCIQMC)[3,4] and its variants (iFCIQMC,[5] S-FCIQMC[6]) adopt the stochastic walker representation of wave functions in the second quantization which is updated in each iteration according to the Hamiltonian operator; convergence is guaranteed in the sense of the inexact power method.[7] Configuration interaction by perturbatively selecting iteration (CIPSI),[8] adaptive configuration interaction (ACI),[9] adaptive sampling configuration interaction (ASCI),[10,11] heat-bath configuration interaction (HCI),[12] and stochastic HCI (SHCI)[13] dynamically select important configurations according to various approximations of the perturbation and then provide variational solutions via traditional eigensolvers together with a post-perturbation estimation of the ground-state energy. Coordinate descent full configuration interaction (CDFCI)[14] reformulates the FCI problem as an unconstrained optimization problem and variationally solves it via a coordinate descent method with hard thresholding. The systematic full configuration interaction fast randomized iteration (sFCI-FRI)[15] applies a fast randomized iteration framework[16] to FCI problems and introduces a hierarchical factorization to further reduce the computational cost. Several other methods[16−19] attempting to solve FCI problems are developed from the numerical linear algebra community. Nevertheless, none of the aforementioned methods can give accurate results for basis sets of size beyond a few dozen, due to the exponential scaling of the computational cost with respect to the basis set size.

FCI solvers, viewed as post-Hartree−Fock (HF) methods, usually adopt molecular orbitals (one-electron and two-electron integrals) from HF calculation and solve the many-body problem starting from there. Thanks to the rotation applied to the basis set (in most cases atomic orbitals) in HF calculation,

Received: June 16, 2020
Published: August 6, 2020

ACS Publications

https://dx.doi.org/10.1021/acs.jctc.0c00613
J. Chem. Theory Comput. 2020, 16, 6207−6221

the molecular orbitals usually give compressible representation of the many-body wave function. In order to further boost the compressibility, one may consider embedding the FCI solver in another loop of orbital rotation.[11] The procedure used in Tubman et al.[11] can be described as follows. Given a set of orbitals, they first apply the FCI solver to generate a rough approximation of the ground-state wave function and its associated one-body density matrix (1RDM). Then these orbitals are rotated via the eigenvectors of the 1RDM. The rotated orbitals are known as the natural orbitals. Using the rotated orbitals (rotated one-body and two-body integrals), the FCI solver is applied again. These two steps are performed repeatedly until some stopping criterion is achieved. This procedure aims to produce orbitals with better compressibility in representing the many-body wave function. The optimality of the natural orbital has been questioned in several works,[20−23] which proposed various optimization procedures under different definitions of optimalities. One shortcoming of all these works, however, is that all these orbital rotations build on top of the many-body wave function with orbitals of the same size as that of the original molecular orbitals; thus, it does not save much computational cost when we start with a large basis set.

In this paper, we consider the following problem: Given a large basis set and limited memory and computational power, what is the optimal variational ground-state energy under the FCI framework? More specifically, let us consider a system with n_e electrons. An HF calculation with a basis set provides the molecular orbitals of size M, $\{\psi_1, ..., \psi_M\}$. Under the restriction of memory usage and computational power, we assume that the FCI solver is only able to solve the FCI problem with N orbitals, where $N < M$. Our goal is then to find a partial unitary matrix $U \in \mathbb{R}^{M\times N}$ such that the ground-state energy is minimized under an optimal set of orbitals of size N, generated from the partial unitary transform of $\{\psi_1, ..., \psi_M\}$ via U. For simplicity we assume that the orbitals are real valued functions and the partial unitary matrix is a real matrix. Such an optimal orbital selection procedure is not only valuable to FCI computations on classical computers but also to FCI computations on noisy intermediate-scale quantum computers.[24,25] Due to the limited number of computational qubits in current quantum computers, compression of orbitals is very much desired.

Although starting from different perspectives, this problem ends up pursuing the same goal as the complete active space self-consistent field method (CASSCF).[26−42] CASSCF is a complete active space version of multiconfigurational self-consistent field (MCSCF) method, which aims to extend the Hartree−Fock calculation to multiconfigurational spaces. Hence, comparing CASSCF and the goal of this paper, CASSCF is proposed starting from extending the Hartree−Fock computational whereas the latter is proposed starting from compressing the FCI computation. Both reach the same place. CASSCF has been rapidly developed for several decades. There are two popular algorithms,[26,33] i.e., the super-CI method[27,43] and the Newton method.[28] The super-CI method solves the first order variational condition with respect to the FCI coefficients and orbitals[43] and results in solving an FCI problem in the active space and an eigenvalue problem in parametrized singly excited states. The Newton method converts the problem to an unconstrained optimization problem and solves it using the Newton method. Since both methods adopt local approximation of the rotation matrix, efficiency is guaranteed only locally. (The two methods will be recalled and presented from an optimization point of view below.) Recently, several modified schemes are developed to further accelerate the orbital minimization.[32,39,41] Other related developments in CASSCF replace the direct FCI solver by the modern FCI solvers mentioned above.[30−32,34−38,40,42] Although targeting the same problem as CASSCF, since the starting points are quite different, we pursue effective algorithms under the setting that FCI solvers are computationally much more expensive compared to the orbital optimization. Such a setting is natural when applying modern FCI solvers to large active orbital spaces and when solving FCI problems on a quantum computer. Our proposed formulas and algorithm, hence, are different from conventional CASSCF algorithms.[26,27] Instead of proposing an ansatz for the rotation matrix and truncating the expression, we optimize the rotation matrix directly through a constrained optimization solver such that the orbital optimization can converge to a minimizer far away from the initial point achieving a better energy. The better orbital optimization potentially reduces the number of macro iterations, which is the total number of solving FCI problems in the active space, and avoids some local minima. Numerically, we find that the macro iteration number in our method either is reduced or remains unchanged compared to that of CASSCF. In our experiments, ground-state energies obtained by OptOrbFCI are always equal or lower than those of CASSCF.

The contribution of our work can be summarized into three parts. First, we mathematically formulate the problem as a constrained optimization problem with two variables: a partial unitary matrix U and the ground-state wave function. Since these two variables are coupled together, the optimization problem is very difficult to solve directly. Hence we adopt the alternating minimization idea. The optimization problem is then decoupled into two single variable optimization problems and solved in an alternating way. Second, we propose an efficient algorithm, namely, OptOrbFCI, for the optimization problem based on the trials of several possible solvers for each of the single variable optimization problems. Specifically CDFCI[14] is applied as the FCI solver, which has not been applied in CASSCF before. Finally, we apply the algorithm to the water molecule, carbon dimer, and nitrogen dimer. Limited by the size of the cc-pVDZ basis set (the number of molecular orbitals from the HF calculation with cc-pVDZ basis set), we produce the variational ground-state energy using the optimal orbitals selected from the cc-pVTZ, cc-pVQZ, and cc-pV5Z basis sets. In all cases, significant improvements of accuracy have been observed. Moreover, the binding curve of the nitrogen dimer is produced using the optimal orbitals selected from the cc-pVQZ basis set limited to the size 28. The dissociation energy is much more accurate than the FCI results under the cc-pVDZ basis set.

The rest of the paper is organized as follows. Section 2 formulates the constrained optimization problem together with two single variable subproblems. The detailed algorithm is introduced in Section 3. In Section 4, we apply OptOrbFCI to the water molecule, carbon dimer, and nitrogen dimer to demonstrate the efficiency of the algorithm. Finally, Section 5 concludes the paper together with a discussion of future work.

2. FORMULATION

This section formulates the problem raised in the Introduction as an optimization problem and derives the related two subproblems.

We first introduce notations used throughout this paper. As before, M and N denote the number of the given molecular orbitals and the computationally affordable number of orbitals

($N < M$). The given large orbital set is $\{\psi_1, ..., \psi_M\}$, and the associated Hamiltonian operator in the second quantization is

$$\hat{H} = \sum_{p,q=1}^{M} h_{pq}\hat{c}_p^\dagger\hat{c}_q + \frac{1}{2}\sum_{p,q,r,s=1}^{M} v_{pqrs}\hat{c}_p^\dagger\hat{c}_q^\dagger\hat{c}_s\hat{c}_r \tag{1}$$

where $\hat{c}_p^\dagger$ and $\hat{c}_q$ are the creation and annihilation operators associated with ψ_p and ψ_q, respectively. The one-electron and two-electron integrals, h_{pq} and v_{pqrs}, admit the following expressions:

$$h_{pq} = \int \mathrm{d}\boldsymbol{x}_1\, \psi_p^*(\boldsymbol{x}_1)h(\boldsymbol{x}_1)\psi_q(\boldsymbol{x}_1) \tag{2}$$

$$v_{pqrs} = \int \mathrm{d}\boldsymbol{x}_1\, \mathrm{d}\boldsymbol{x}_2\, \psi_p^*(\boldsymbol{x}_1)\psi_q^*(\boldsymbol{x}_2)v(\boldsymbol{x}_1, \boldsymbol{x}_2)\psi_s(\boldsymbol{x}_2)\psi_r(\boldsymbol{x}_1) \tag{3}$$

where $h(\boldsymbol{x}_1)$ and $v(\boldsymbol{x}_1, \boldsymbol{x}_2)$ are the one-body and two-body operators, respectively. Due to the limited memory and computational power, we are only able to solve FCI problems under N orbitals. Hence, we introduce a partial unitary matrix $U \in \mathcal{U}(M, N)$, where $\mathcal{U}(M, N)$ is the space of all partial unitary matrix of size M by N, i.e.,

$$\mathcal{U}(M, N) = \{U \in \mathbb{R}^{M\times N} | U^{\mathrm{T}}U = I_N\} \tag{4}$$

and I_N denotes the identity matrix of size N by N. The transformed orbitals from $\{\psi_1, ..., \psi_M\}$ via U are denoted as $\{\phi_1, ..., \phi_N\}$ such that

$$\phi_i = \sum_{j=1}^{M} \psi_j U_{ji} \tag{5}$$

where U_{ji} denotes the (j, i)th entry of U. We also adopt the expression $(\phi_1, ..., \phi_N) = (\psi_1, ..., \psi_M)\ U$ to denote the transformation. The Hamiltonian operator associated with $\{\phi_1, ..., \phi_N\}$ is then

$$\tilde{H} = \sum_{p',q'=1}^{N} \tilde{h}_{p'q'}\hat{\boldsymbol{d}}_{p'}^\dagger\hat{\boldsymbol{d}}_{q'} + \frac{1}{2}\sum_{p',q',r',s'=1}^{N} \tilde{v}_{p'q'r's'}\hat{\boldsymbol{d}}_{p'}^\dagger\hat{\boldsymbol{d}}_{q'}^\dagger\hat{\boldsymbol{d}}_{s'}\hat{\boldsymbol{d}}_{r'} \tag{6}$$

where $\hat{\boldsymbol{d}}_{p'}^\dagger$ and $\hat{\boldsymbol{d}}_{q'}$ are the creation and annihilation operators associated with $\phi_{p'}$ and $\phi_{q'}$ respectively, the one-electron integral $\tilde{h}_{p'q'}$ is

$$\begin{aligned}\tilde{h}_{p'q'} &= \int \mathrm{d}\boldsymbol{x}_1\, \phi_{p'}^*(\boldsymbol{x}_1)h(\boldsymbol{x}_1)\phi_{q'}(\boldsymbol{x}_1)\\ &= \sum_{p,q=1}^{M} h_{pq}U_{pp'}U_{qq'}\end{aligned} \tag{7}$$

and the two-electron integral $\tilde{v}_{p'q'r's'}$ is

$$\begin{aligned}\tilde{v}_{p'q'r's'} &= \int \mathrm{d}\boldsymbol{x}_1\, \mathrm{d}\boldsymbol{x}_2\, \phi_{p'}^*(\boldsymbol{x}_1)\phi_{q'}^*(\boldsymbol{x}_2)v(\boldsymbol{x}_1, \boldsymbol{x}_2)\phi_{s'}(\boldsymbol{x}_2)\phi_{r'}(\boldsymbol{x}_1)\\ &= \sum_{p,q,r,s=1}^{M} v_{pqrs}U_{pp'}U_{qq'}U_{ss'}U_{rr'}\end{aligned} \tag{8}$$

The connection (eq 5) between orbital set $\{\psi_1, ..., \psi_M\}$ and $\{\phi_1, ..., \phi_N\}$ implies the connection between annihilation operators,

$$\hat{\boldsymbol{d}}_{q'} = \sum_{q=1}^{M} \hat{c}_q U_{qq'} \tag{9}$$

Such a relationship also holds for creation operators.

Moreover, we denote the variational space for wave function as $\mathcal{D}[(\phi_1, ..., \phi_N)] = \mathcal{D}[(\psi_1, ..., \psi_M)U]$, which is the span of all Slater determinants constructed from $\{\phi_1, ..., \phi_N\}$.

With all notations defined above, our problem can be formulated as

$$\min_{\substack{|\Phi\rangle\in\mathcal{D}[(\psi_1,...,\psi_M)U]\\ \langle\Phi|\Phi\rangle=1\\ U\in\mathcal{U}(M,N)}} \langle\Phi|\hat{H}|\Phi\rangle \tag{10}$$

Notice the second quantization form of $\hat{H}$ is under the orbital set $\{\psi_1, ..., \psi_M\}$ whereas the wave function $|\Phi\rangle$ lives in the variational space associated with $\{\phi_1, ..., \phi_N\}$. Such an inconsistency is inconvenient to handle numerically.

We now show that it is in fact equivalent to replace the Hamiltonian $\hat{H}$ in eq 10 by $\tilde{H}$; thus, both the Hamiltonian and the wave function are associated with the same set of orbitals $\{\phi_1, ..., \phi_N\}$. The connection between $\hat{\boldsymbol{d}}_{q'}$ and $\hat{c}_q$ in eq 9 leads to the anticommutation relation between $\hat{\boldsymbol{d}}_{p'}^\dagger$ and $\hat{c}_q$,

$$\{\hat{c}_q, \hat{\boldsymbol{d}}_{p'}^\dagger\} = \sum_{p=1}^{M} \{\hat{c}_q, \hat{c}_p^\dagger\}U_{pp'} = U_{qp'} \tag{11}$$

Define another operator $\tilde{c}_q = \sum_{q'=1}^{N}\hat{\boldsymbol{d}}_{q'}U_{qq'}$. The anticommutation relation between $\hat{\boldsymbol{d}}_{p'}^\dagger$ and $\tilde{c}_q$ is the same as eq 11,

$$\{\tilde{c}_q, \hat{\boldsymbol{d}}_{p'}^\dagger\} = \sum_{q'=1}^{N} \{\hat{\boldsymbol{d}}_{q'}, \hat{\boldsymbol{d}}_{p'}^\dagger\}U_{qq'} = U_{qp'} \tag{12}$$

Since both $\hat{c}_q$ and $\tilde{c}_q$ have the same anticommutation relation with $\hat{\boldsymbol{d}}_{p'}^\dagger$, these two annihilation operators acting on any wave function $|\Phi\rangle$ in $\mathcal{D}[(\psi_1, ..., \psi_M)U]$ give the same results, i.e.,

$$\hat{c}_q|\Phi\rangle = \tilde{c}_q|\Phi\rangle \tag{13}$$

Hence, the objective function $\langle\Phi|\hat{H}|\Phi\rangle$ in eq 10 admits the same result if all creation and annihilation operators are replaced by $\tilde{c}_p^\dagger$ and $\tilde{c}_q$. The resulting Hamiltonian is exactly $\tilde{H}$ associated with $\{\phi_1, ..., \phi_N\}$ defined in eq 6. A more detailed derivation can be found in Appendix A. Our problem (eq 10), thus, is equivalent to,

$$\min_{\substack{|\Phi\rangle\in\mathcal{D}[(\psi_1,...,\psi_M)U]\\ \langle\Phi|\Phi\rangle=1\\ U\in\mathcal{U}(M,N)}} \langle\Phi|\tilde{H}[U]|\Phi\rangle \tag{14}$$

where $\tilde{H}[U]$ is $\tilde{H}$ defined in eq 6, and we write U in brackets to emphasize its dependency on U.

Remark 2.1. *If we assume that, under optimal orbital selection, the system with a smaller number of electrons has higher energy, then it can be shown that eq 14 is equivalent to the following problem:*

$$\min_{\substack{|\Psi\rangle\in\mathcal{D}[(\psi_1,...,\psi_M)]\\ \langle\Psi|\Psi\rangle=1\\ U\in\mathcal{U}(M,N)}} \langle\Psi|\tilde{H}[U]|\Psi\rangle \tag{15}$$

where the wave function $|\Psi\rangle$ now lives in a larger variational space (and thus the computational cost exceeds the limitation). We shall focus on the surrogate problem (14), which is computationally feasible.

The objective function in our original problem (eq 10) has the same expression as that in the FCI problem under the orbital set $\{\psi_1, ..., \psi_M\}$. Moreover, any feasible wave function in eq 10 belongs to the space $\mathcal{D}[(\psi_1, ..., \psi_M)]$, which is the variational space of the FCI problem under $\{\psi_1, ..., \psi_M\}$. Since the FCI problem under $\{\psi_1, ..., \psi_M\}$ is a variational method for the many-body Schrödinger equation, our problem (eq 10) is also a variational method and so is eq 14. Therefore, solving eq 14 gives a variational ground-state energy and its wave function.

We see that $|\Phi\rangle$ and U in eq 14 are coupled together. Instead of minimizing $|\Phi\rangle$ and U simultaneously, we minimize eq 14 in an alternating fashion. We first fix U and minimize eq 14 with respect to $|\Phi\rangle$ only. Once the minimizer of $|\Phi\rangle$ is achieved, we then fix $|\Phi\rangle$ and minimize eq 14 with respect to U only. The procedure is repeated until some convergence criterion is achieved. Next, we derive the two subproblems for fixed U and fixed $|\Phi\rangle$, respectively.

Subproblem with Fixed *U*. When we fix U in eq 14, the orbital set $\{\phi_1, ..., \phi_N\}$ is also fixed. The optimization problem (eq 14) is then simplified as

$$\min_{\substack{|\Phi\rangle \in \mathcal{D}[(\phi_1,...,\phi_N)] \\ \langle\Phi|\Phi\rangle=1}} \langle\Phi|\tilde{H}|\Phi\rangle \tag{16}$$

which is a standard FCI problem under the orbital set $\{\phi_1, ..., \phi_N\}$.

Subproblem with Fixed $|\Phi\rangle$. When we fix $|\Phi\rangle$, the objective function in eq 14) can be written as

$$\begin{aligned}\langle\Phi|\tilde{H}[U]|\Phi\rangle &= \sum_{p',q'=1}^{N} \tilde{h}_{p'q'}\langle\Phi|\hat{\boldsymbol{d}}_{p'}^{\dagger}\hat{\boldsymbol{d}}_{q'}|\Phi\rangle \\ &\quad + \sum_{p',q',r',s'=1}^{N} \tilde{v}_{p'q'r's'}\langle\Phi|\hat{\boldsymbol{d}}_{p'}^{\dagger}\hat{\boldsymbol{d}}_{q'}^{\dagger}\hat{\boldsymbol{d}}_{s'}\hat{\boldsymbol{d}}_{r'}|\Phi\rangle \\ &= \sum_{p',q'=1}^{N}\sum_{p,q=1}^{M} h_{pq}U_{pp'}U_{qq'}\,{}^{1}D_{q'}^{p'} \\ &\quad + \sum_{p',q',r',s'=1}^{N}\sum_{p,q,r,s=1}^{M} v_{pqrs}U_{pp'}U_{qq'}U_{rr'}U_{ss'}\,{}^{2}D_{r's'}^{p'q'} \\ &=: P_4(U)\end{aligned} \tag{17}$$

where ${}^{1}D_{q'}^{p'} = \langle\Phi|\hat{\boldsymbol{d}}_{p'}^{\dagger}\hat{\boldsymbol{d}}_{q'}|\Phi\rangle$ and ${}^{2}D_{r's'}^{p'q'} = \langle\Phi|\hat{\boldsymbol{d}}_{p'}^{\dagger}\hat{\boldsymbol{d}}_{q'}^{\dagger}\hat{\boldsymbol{d}}_{s'}\hat{\boldsymbol{d}}_{r'}|\Phi\rangle$ are the standard one-body reduced density matrix (1RDM) and two-body reduced density matrix (2RDM), respectively. The objective function, denoted as $P_4(U)$, is then a fourth order polynomial of U. Notice that h_{pq} and v_{pqrs} are given coefficients associated with the original molecular orbital set $\{\psi_1, ..., \psi_M\}$, and ${}^{1}D_{q'}^{p'}$ and ${}^{2}D_{r's'}^{p'q'}$ are also independent of U as long as we fix $|\Phi\rangle$. Hence the subproblem can be summarized as

$$\min_{U \in \mathcal{U}(M,N)} P_4(U) \tag{18}$$

which minimizes a fourth order polynomial of U with an orthonormality constraint.

3. ALGORITHM

In this section, we will first discuss algorithms for solving eqs 16 and 18 in Section 3.1 and Section 3.2, respectively. Then the overall algorithm, OptOrbFCI, is summarized as a pseudo-code in Section 3.3 together with some discussion on initial guesses, convergence, stopping criteria, and computational complexities.

3.1. FCI Solvers and RDM Methods.

Algorithms in this section aim for solving the FCI problem (eq 16) and producing 1RDM and 2RDM as inputs for eq 18. Most FCI solvers can produce RDMs. The potential choices then include but are not limited to DMRG,[1,2] FCIQMC,[3] ACI,[9] HCI,[12] and CDFCI.[14] The perturbation energy is not needed for intermediate iterations and is optional for the last FCI solved in OptOrbFCI. Throughout this paper, CDFCI is the solver used to address all FCI problems.

Regarding 1RDM and 2RDM, the computational cost is on the same order as applying the Hamiltonian operator to the many-body wave function one time, while, due to the efficiency of CDFCI, the runtime for the FCI solving part is also of the same order. Hence the computation of RDMs needs to be carefully addressed. Since 1RDM can be easily reduced from 2RDM with cheap computational cost, we focus only on the computation of 2RDM here. Assume the wave function is of the form $|\Phi\rangle = \sum_{i \in \mathcal{I}} x_i |D_i\rangle$, where $|D_i\rangle$ denotes a Slater determinant in $\mathcal{D}[(\phi_1, ..., \phi_N)]$, x_i is the corresponding coefficient, and $\mathcal{I}$ denotes the index set of nonzero coefficients, i.e., $x_i \neq 0$ for all $i \in \mathcal{I}$. We introduce two methods for computing 2RDM.

The first method is of quadratic scaling with respect to the cardinality of $\mathcal{I}$, $|\mathcal{I}|$. It loops over all pairs of Slater determinants with nonzero coefficients, i.e., $(|D_i\rangle, |D_j\rangle)$ for $i, j \in \mathcal{I}$. If two Slater determinants differ by more than two orbitals, then this pair does not contribute to 2RDM. Otherwise, the contribution to 2RDM is evaluated. Notice that there are only $O(N^2|\mathcal{I}|)$ pairs that contribute to 2RDM and all of the rest of the pairs only require an "XOR" and a "POPCOUNT" (the population count operation counts the number of set bits in a value, which is usually implemented using hardware in modern computers) operation, both of which are of great efficiency in modern computers.

The second method is of linear scaling with respect to $|\mathcal{I}|$. It loops over all Slater determinants with nonzero coefficients. For each determinant, $|D_i\rangle$, it applies all possible $\hat{\boldsymbol{d}}_{p'}^{\dagger}\hat{\boldsymbol{d}}_{q'}^{\dagger}\hat{\boldsymbol{d}}_{s'}\hat{\boldsymbol{d}}_{r'}$ to the determinant and queries the coefficient of $\hat{\boldsymbol{d}}_{p'}^{\dagger}\hat{\boldsymbol{d}}_{q'}^{\dagger}\hat{\boldsymbol{d}}_{s'}\hat{\boldsymbol{d}}_{r'}|D_i\rangle$. The contribution, i.e., the product of the coefficients of both determinants and multiplying the sign, is then added to 2RDM. Unlike the first method, where only $O(|\mathcal{I}|)$ queries of the coefficients of the many-body wave function are needed and then these coefficients are stored and accessed in an array, the second method requires $O(N^2|\mathcal{I}|)$ queries. In almost all FCI solvers, special data structures are used to store the wave function with sparse coefficients, e.g., hash table, black-red tree, sorted array, etc. Querying any of these special data structures is relatively expensive. Hence the runtime of the second method is much slower than that of the first one if $|\mathcal{I}|$ is not large.

In practice, we dynamically select the method to compute 2RDM based on both $|\mathcal{I}|$ and the querying cost. Nevertheless, the runtime of the second method is guaranteed to be of the same order as the FCI solving part in CDFCI. Hence the overall total runtime for solving eq 16 and producing RDMs is, in general, no more than twice of the FCI solver runtime in CDFCI.

3.2. Optimizing the Orthonormal Constrained Polynomial.

This section introduces the algorithm used to solve eq 18. Although the objective function is simply a fourth order polynomial of U, the orthonormality constraint makes the problem in general more difficult to solve than the linear eigenvalue problem. Luckily, the variable U is only of dimension $M \times N$. Comparing to the FCI problem, which usually costs $O\left(\binom{N}{n_e}\right)$ operations, the computational cost of minimizing eq 18, in most cases, is negligible, while the efficient algorithm is

https://dx.doi.org/10.1021/acs.jctc.0c00613
J. Chem. Theory Comput. 2020, 16, 6207−6221

still desired, especially when the given molecular orbital set size M is much larger than N.

Regarding the orthonormality constrained optimization problems, there are three major groups of techniques to deal with the constraint, namely, augmented Lagrangian methods,[44,45] projection methods,[46] and manifold based methods.[47,48] For these methods, we explored the efficiency on a small test problem and employ a projection method with alternating Barzilai−Borwein (BB) stepsize.[46]

The iteration for the employed method can be written as

$$U_{k+1} = \mathrm{orth}(U_k - \tau_k \nabla_U P_4(U_k)) \tag{19}$$

where U_k denotes the U matrix at the kth iteration, $\mathrm{orth}(\cdot)$ denotes the orthonormalization function, and τ_k is the alternating BB stepsize. The orthonormalization function of any matrix V is defined as the orthonormal basis of V and implemented as

$$\mathrm{orth}(V) = VQ\Lambda^{-1/2}$$

where Q and Λ are eigenvectors and eigenvalues of $V^{\mathrm{T}}V$, i.e., $V^{\mathrm{T}}V = Q\Lambda Q^{\mathrm{T}}$. The alternating BB stepsize applies two BB stepsizes in an alternating way as,

$$\tau_k = \begin{cases} \tau_k^{\mathrm{BB1}} & \text{for odd } k \\ \tau_k^{\mathrm{BB2}} & \text{for even } k \end{cases}$$

where

$$\tau_k^{\mathrm{BB1}} = \frac{\langle U_k - U_{k-1}, U_k - U_{k-1}\rangle}{|\langle U_k - U_{k-1}, G_k - G_{k-1}\rangle|}$$

$$\tau_k^{\mathrm{BB2}} = \frac{|\langle U_k - U_{k-1}, G_k - G_{k-1}\rangle|}{\langle G_k - G_{k-1}, G_k - G_{k-1}\rangle}$$

$G_k = \nabla_U P_4(U_k)$ is the gradient of P_4 at U_k, and $\langle A, B\rangle = \mathrm{tr}\, A^{\mathrm{T}}B$.

3.3. OptOrbFCI.

The overall algorithm, OptOrbFCI, hence, alternatively minimizes eqs 16 and 18, with some computations to prepare the inputs for each other. We summarize OptOrbFCI as follows.

Step 1: Set iteration index $k = 0$ and prepare initial guess U_0.
Step 2: Calculate the reduced one-body and two-body integrals using U_k as eqs 7 and 8, respectively.
Step 3: Solve the FCI problem (eq 16) via the CDFCI method and obtain the ground-state wave function and energy.
Step 4: If the decay of the ground-state energy is smaller than the given tolerance, convergence has been achieved and the algorithm is stopped.
Step 5: Compute the 1RDM and 2RDM from the ground-state wave function.
Step 6: Solve the orthonormal constrained polynomial (eq 18) via projection method with alternating BB stepsize as eq 19 and obtain U_{k+1}.
Step 7: Set $k = k + 1$ and repeat Steps 2−7.

Notice in the above algorithm that the stopping criteria are checked right after the FCI calculation rather than at the end of each iteration. However, it is not activated until the second iteration so that we can compare the FCI ground-state energies of the current iteration against those of the previous iteration. We also emphasize that the CDFCI method employed here is just one choice of FCI solvers. OptOrbFCI can employ many other FCI solvers as a replacement.

In the following, we discuss some details of the algorithm, i.e., initial guesses, convergence, stopping criteria, and computational complexities.

Initial Guesses. In OptOrbFCI, the only variable needed to be initialized is U_0. We found that using a random orthonormal matrix as the initialization of U_0 works in practice, while, in this case, the FCI ground-state energy in the first iteration is even worse than the HF energy. A better initialization for U_0, which is the one used throughout all numerical experiments in this paper, is the permutation matrix selecting N different orbitals with the lowest HF orbital energy from $\{\psi_1, ..., \psi_M\}$.

Besides the initialization for the overall algorithm, we also need to give initializations for both subproblems, eqs 16 and 18. For eq 16, in regular CDFCI, the wave function is usually initialized as the single HF state. However, after rotation via U, we lose track of the HF state in the new orbital set, $\{\phi_1, ..., \phi_N\}$. Hence we initialize CDFCI as a single state with $\frac{n_e}{2}$ orbitals with smallest "orbital energy" doubly occupied (spin-up and spin-down), where the "orbital energy" of $\phi_{p'}$ is defined as

$$\sum_p \varepsilon_p U_{pp'}^2 \tag{20}$$

where ε_j is the orbital energy of ψ_p. The initial guess for eq 18 at iteration k, denoted as $U_k^{(0)}$, is the convergent orthonormal matrix U_{k-1} from the previous iteration with a small random perturbation, i.e.,

$$U_k^{(0)} = \mathrm{orth}(U_{k-1} + \mathrm{rand}(M, N)) \tag{21}$$

where $\mathrm{rand}(M, N)$ denotes a random matrix of size M by N with each entry sampled from normal distribution with mean 0 and standard deviation 0.1. Using such an initial guess, the convergence is empirically found much faster than that using a purely random initial guess. Adding randomness to the initial guess in many cases helps with escaping from local minima. A similar observation is obtained by the stochastic CASSCF method,[35,49] where the randomness is added to RDMs via FCIQMC. We emphasize that this is a crucial point making our method achieve a lower ground-state energy than conventional CASSCF methods.

Convergence. We first discuss the convergence of solving eqs 16 and 18 and then move to the discussion on the convergence of OptOrbFCI.

The convergence of the CDFCI algorithm in solving eq 16 is discussed in detail in Li et al.[17] Since CDFCI rewrites the linear eigenvalue problem as an unconstrained optimization problem with a nonconvex objective function, the global convergence is guaranteed without a rate and the local convergence with a linear rate is also proved in the compression-free setting.

The convergence analysis of the projection method with alternating BB stepsize is proposed in Gao et al.[46] for solving general orthonormal constrained optimization problems, which include our subproblem (eq 18). This method is guaranteed to converge to points with a first-order optimality condition; i.e., these points have a vanishing gradient along the tangent plane of the constraint.

The convergence analysis of OptOrbFCI has not been rigorously shown and is beyond the scope of this paper. However, the rich literature in the convergence analysis of the alternating direction method of multipliers[50] and coordinate-wise descent methods[17,51−53] sheds light on the analysis of OptOrbFCI. In general, the convergence analysis of the overall alternating algorithm relies on the convergence analysis of subproblems and the property of the overall objective function. If we apply the alternating algorithm to eq 15, since the space of $|\Phi\rangle$ remains unchanged, the energy is guaranteed to decrease monotonically. Hence, if we have the equivalence between eq 14 and eq 15 for all U, then we also have a monotone decreasing property for solving eq 14. Together with the convergence properties of both subproblems, we know that OptOrbFCI converges to points with a first-order optimality condition.

Stopping Criteria. There are plenty choices of stopping criteria for each of three iterative algorithms. In practice, we use the following stopping criteria joined with a fixed maximum number of iterations.

In CDFCI, we monitor the exponential moving average of the norm of the coefficient difference, i.e.,

$$S_t = (1 - \alpha)\|\Delta x_t\| + \alpha S_{t-1} \tag{22}$$

where t is the iteration index, $\alpha = 0.99$ is the decay factor, Δx_t denotes the coefficient difference, and S_t is the moving average. CDFCI stops if S_t is smaller than a given tolerance.

The stopping criterion of the projection method for the subproblem with fixed U is similar, i.e.,

$$S_t = (1 - \alpha)|\Delta E_t| + \alpha S_{t-1} \tag{23}$$

where ΔE_t is the difference of objective functions $P_4(U_t)$ and $P_4(U_{t-1})$ and $\alpha = 0.8$ is the decay factor. If S_t is smaller than a given tolerance, we stop the projection method.

In OptOrbFCI, we observe monotone decay of the FCI energy. Hence the algorithm stops if the per-iteration decay is smaller than a given tolerance.

Computational Complexities. The computational complexity for an iterative algorithm depends on both the per-iteration complexity and the number of iterations. Our discussion also follows these two parts.

For the CDFCI algorithm, each iteration applies the Hamiltonian operator to a single Slater determinant. The per-iteration computational cost is dominated by the double excitation part, which selects two electrons and excites them to two unoccupied orbitals. Hence, CDFCI costs $O(N^2 n_e^2)$ operations per iteration. However, the number of iterations is usually big, which is still believed to be of the order $O\left(\binom{N}{n_e}\right)$ with a small prefactor. In practice, the iteration number is usually around 10^6 to 10^8 for small systems we have tested to achieve 10^{-1} mHa accuracy. The computational complexity in producing RDMs is similar to that of the CDFCI solver part.

For the projection method, each iteration computes the gradient of the objective function, whose computational cost is dominated by contracting a four-way tensor v_{pqrs} with a U matrix in three dimensions. The per iteration, hence, costs $O(M^4 N)$ operations. The number of iterations is much smaller than that in CDFCI. For systems we have tested, iteration numbers are around a few hundreds to a few thousands for the first two iterations in the overall algorithm. Starting from the third iteration, the iteration number of the projection method quickly drops to a couple hundred depending on the level of random perturbation on the initial value.

Putting the computational complexity for both CDFCI and the projection method together, we have a per-iteration cost for OptOrbFCI. When M is not much bigger than N, the CDFCI part dominates the computation cost and the projection method part can be ignored. However, when M is much bigger than N, e.g., when the cc-pV5Z basis set is used, the computational cost of the projection method is not negligible, but the CDFCI part is still more expensive. Regarding the iteration number, OptOrbFCI usually achieves chemical accuracy in a few iterations. The convergence to an accuracy 10^{-2} mHa can also be achieved within two dozen iterations for all the cases we have tested.

3.4. Comparison with CASSCF Algorithms.

We compare OptOrbFCI with two conventional CASSCF algorithms, i.e., the Newton−Raphson[27] and super-CI methods.[26,28] In the following, we first briefly review these two methods, in particular from an optimization point of view, and then compare them with our proposed OptOrbFCI algorithm.

Conventional CASSCF algorithms start with a different representation for the orbital rotation matrix. Recall that OptOrbFCI directly deals with the partial unitary matrix with an orthonormality constraint. While in the CASSCF framework, the orbital rotation is given by a square unitary matrix U parametrized as

$$U = e^X \tag{24}$$

with X being a skew-symmetric matrix. We denote the Slater determinant of orbitals $\{\psi_1, ..., \psi_N\}$ as $\{|D_i\rangle\}$, so a wave function $|\Psi\rangle \in \mathcal{D}[(\psi_1, ..., \psi_N)]$ (recall that $\mathcal{D}[(\psi_1, ..., \psi_N)]$ is the space spanned by Slater determinants given by $\{\psi_1, ..., \psi_N\}$) can be written as

$$|\Psi\rangle = \sum_{i \in \mathcal{I}} x_i |D_i\rangle \tag{25}$$

where x_i are linear combination coefficients and $\mathcal{I}$ denotes the set of all configurations out of N orbitals. The target wave function after rotation is then given by

$$|\Phi\rangle = \hat{U}|\Psi\rangle = e^{\hat{X}}|\Psi\rangle \tag{26}$$

where $\hat{U} = e^{\hat{X}}$ denotes the rotation operator on the Slater determinants (and hence the span) corresponding to $U = e^X$ in eq 24.

From the point of view of optimization, the Newton−Raphson method first converts eq 14 to an unconstrained optimization problem using eq 24 for the orbital rotation matrix, given by

$$\min_{X, \{x_i\}: \|x\| = 1} E(X, \{x_i\}) \tag{27}$$

with

$$E(X, \{x_i\}) = \langle \Psi | e^{-\hat{X}} \hat{H} e^{\hat{X}} | \Psi \rangle \tag{28}$$

where Ψ is given by eq 25, so that $\|x\| = 1$ is equivalent to the normality constraint for $|\Phi\rangle$ due to the orthonormality between Slater determinants. Note that with fixing X, the optimization of E with respect to $\{x_i\}$ leads to a standard eigenvalue problem; hence, the exact optimum can be obtained via FCI solvers, similar to OptOrbFCI. The optimization with respect to X becomes unconstrained, so the standard second order optimization method can be applied. However, as a price to pay, the dependence of E on X becomes quite complicated due to the parametrization (eq 24). In the Newton−Raphson method, one approximates $E(X)$ quadratically near $X = 0$. The optimization of X using the surrogate quadratic approximation leads to the linear system

$$\left.\frac{\partial E}{\partial X_{pq}}\right|_0 + \sum_{r<s} \left.\frac{\partial^2 E}{\partial X_{pq} \partial X_{rs}}\right|_0 X_{rs} = 0 \tag{29}$$

To write down the equation more explicitly, let us introduce a short-hand notation for the singly excited state as

$$|pq\rangle = (\hat{c}_p^\dagger \hat{c}_q - \hat{c}_q^\dagger \hat{c}_p)|\Psi\rangle \tag{30}$$

Then the first order derivative at $X = 0$ reads

$$\left.\frac{\partial E}{\partial X_{pq}}\right|_0 = 2\langle\Psi|\hat{H}|pq\rangle \tag{31}$$

and the second order derivative reads

$$\left.\frac{\partial^2 E}{\partial X_{pq}\partial X_{rs}}\right|_0 = 2\langle pq|\hat{H}|rs\rangle + \langle pq|(\hat{c}_s^\dagger \hat{c}_r - \hat{c}_r^\dagger \hat{c}_s)\hat{H}|\Psi\rangle + \langle rs|(\hat{c}_q^\dagger \hat{c}_p - \hat{c}_p^\dagger \hat{c}_q)\hat{H}|\Psi\rangle \tag{32}$$

After X is obtained in each macro iteration, the orbitals are rotated based on X.[26,27,54] When the exact Hessian is used and the rotation based on X is handled carefully (so that it is at least second order accurate for small X), the Newton−Raphson method has local quadratic convergence.[54]

The super-CI method takes a slightly different point of view by directly taking an expansion of eq 26 (instead of E) with respect to X. The first order approximation of $e^{\hat{X}}|\Psi\rangle$ is known as the singly excited wave function as

$$|\Psi_{\text{SCI}}\rangle = |\Psi\rangle + \sum_{r<s} X_{rs}(\hat{c}_r^\dagger \hat{c}_s - \hat{c}_s^\dagger \hat{c}_r)|\Psi\rangle \tag{33}$$

where the subscript SCI is short for singly excited CI. To determine X, the energy of $|\Psi_{\text{SCI}}\rangle$ is minimized; as it is not necessarily normalized, we minimize the Ritz value

$$\frac{\langle\Psi_{\text{SCI}}|\hat{H}|\Psi_{\text{SCI}}\rangle}{\langle\Psi_{\text{SCI}}|\Psi_{\text{SCI}}\rangle}$$

with respect to X, which is equivalent to solving the eigenvalue problem of the matrix

$$\begin{bmatrix} \langle\Psi|\hat{H}|\Psi\rangle & \langle\Psi|\hat{H}|rs\rangle \\ \langle pq|\hat{H}|\Psi\rangle & \langle pq|\hat{H}|rs\rangle \end{bmatrix} \tag{34}$$

where the second column and second row are block matrices index by rs and pq, respectively. Thus, each step of super-CI can also be viewed as solving an eigenvalue problem in an extended variational space. Compared with the Newton−Raphson method, the matrix above is related to the Hessian used in the Newton−Raphson method (eq 29). The last two terms in the second derivative (eq 32) are missing in the super-CI matrix, due to the different approximation taken in the expansion.

In both CASSCF algorithms, the rotation of the orbitals according to X needs to be processed very carefully. Direct transformation using the first order approximation of eq 24 is manageable if orbitals are then orthogonalized or an overlapping matrix is introduced. An alternative approach is through the natural orbital of the singly excited wave function $|\Psi_{SCI}\rangle$.

We emphasize that not every element of X is involved in the above calculation. Since the energy E is invariant to the rotation within unselected orbitals, the elements X_{pq} for both p and q corresponding to unselected orbitals are ignored, which also improves the numerical stability of the above algorithms. Moreover the energy E is also invariant to the rotation within selected orbitals. If the direct FCI solver is applied, the elements X_{pq} for both p and q corresponding to selected orbitals can be ignored as well, while, if modern FCI solvers are applied, which all include some compression of the coefficients, the rotation within the selected orbitals often helps improve the compressibility of the wave function coefficients; hence, they are preserved in the calculations.[11,42] In the end, the numbers of degrees of freedom in all three algorithms are the same.

Recall that the energy is only a fourth order polynomial of the unitary matrix U as shown in eq 17, while on the other hand, after introducing the parametrization (eq 24), the energy depends in a quite complicated way on the parameter matrix X. Conventional CASSCF algorithms then introduce approximations to E and $\hat{U}|\Psi\rangle$. Expressions are valid when X is around zero, which means that U is close to an identity matrix. Hence, at each macro step, conventional CASSCF algorithms are valid and efficient if the rotation of orbitals is not far from identity. There are two potential drawbacks of this local optimization: (1) many macro iterations are needed to move the rotation matrix away from its initialization; (2) algorithms converge efficiently to a local minimum close to the initial value. In comparison, OptOrbFCI adopts modern optimization techniques for orthonormal constrained optimization problems and is free to converge to any orthonormal matrix in each macro iteration. Therefore, each orbital optimization problem is solved more accurately and the algorithm potentially converges to better minima with lower energies. Specifically, taking a random initial unitary matrix is feasible in OptOrbFCI, while it leads to unsatisfactory results in conventional CASSCF calculations. The price to pay is possibly a more expensive orbital optimization cost compared with conventional CASSCF algorithms. However, we find that such a cost is negligible compared to the cost of FCI solvers, which is the setting that motivates our work.

Remark 3.1. *In CASSCF, the orbitals are usually split into three groups, inactive, active, and virtual. Active and virtual orbitals correspond to the selected orbitals and unselected ones after rotation. Inactive orbitals are orbitals frozen to be doubly occupied ones. Introducing the inactive orbitals does not change the structure of any optimization algorithm above. With another set of indices denoting the inactive orbitals, many matrix/tensor elements are zeros, which help reduce the computational cost. We omit the related expressions for simplicity.*

4. NUMERICAL RESULTS

In this section, we demonstrate the efficiency of the proposed OptOrbFCI through several numerical experiments. First, we explore the detailed properties of OptOrbFCI through a sequence of numerical experiments on a single water molecule. A comparison against the CASSCF method is explored here as well. Then we compare the ground-state energies of the carbon dimer and nitrogen dimer calculated through OptOrbFCI under various basis sets, i.e., cc-pVDZ, cc-pVTZ, cc-pVQZ, and cc-pV5Z. Finally, we adopt OptOrbFCI to benchmark the binding curve of the nitrogen dimer under the cc-pVQZ basis set, which consists of systems with various levels of correlations. And the dissociation energy for the nitrogen dimer is also compared against that through the FCI method under various basis sets.

In all the numerical experiments, the original given orbitals (one-body and two-body integrals) are calculated via the restricted HF (RHF) in PSI4[55] package. All energies are reported in the unit of Hartree (Ha).

We adopt the modern C++ implementation of CDFCI[56] and our own version of the projection method[46] implemented in MATLAB. Multithread parallelization is disabled in CDFCI. The communication between CDFCI and the projection method is done via file system, i.e., the FCIDUMP file and RDM files. All results labeled by FCI are produced by CDFCI. The implementation of the CASSCF method in PySCF 1.7.1[57] is applied for comparison purposes.

4.1. H_2O Molecule. The water molecule used in this section is at its equilibrium geometry,[3,14] i.e., OH bond length 1.84345a_0 and HOH bond angle 110.6°. Table 1 summarizes the properties associated with different basis sets.

Table 1. Basis Sets for H_2O[a]

molecule	basis	electrons	orbitals	HF energy	GS energy
H_2O	cc-pVDZ	10	24	−76.0240386	−76.2418601
	cc-pVTZ	10	58	−76.0544374	–
	cc-pVQZ	10	115	−76.0621073	–
	cc-pV5Z	10	201	−76.0644002	–

[a] HF energy denotes the Hartree-Fock energy calculated by PSI4[55] and GS energy denotes the FCI ground-state energy calculated by CDFCI.[14] A bar means the number is not available.

For CDFCI, the compression threshold is 5×10^{-7}, the tolerance for convergence is 5×10^{-6}, and the maximum number of iterations is 3×10^{7}. The convergence tolerance for the projection method is 10^{-7}, and the maximum number of iterations is 10^{4}. For OptOrbFCI, the convergence tolerance is 10^{-4} and the maximum number of iterations is 20. These settings are used for all numerical experiments of the H_2O molecule.

Two different numbers of selected orbitals, $N = 12$ and $N = 24$, are tested for H_2O molecules on a sequence of basis sets. Figure 1 and Figure 3 show the convergence behavior of OptOrbFCI against the iteration number for $N = 12$ and $N = 24$, respectively. The HF energies are also plotted in both figures with the x-axis label being "HF". The energies associated with iteration 0 are the FCI energies before applying the projection method, and the orbitals with the smallest N orbital energies are used as the selected orbitals. Figure 2 and Figure 4 further show the log scale of the energy difference against the iteration. Here the energy difference is defined as the difference between the FCI ground-state energy at current iteration and the converged FCI ground-state energy. In Figure 4, the curve associated with cc-pVDZ is removed since the ground-state energies stay constant throughout the iterations. Table 2 lists all convergent FCI ground-state energies.

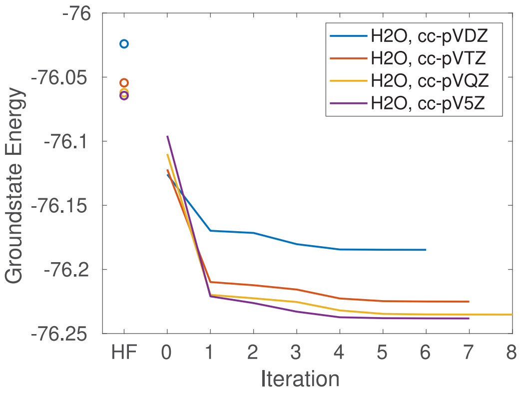

Figure 1. Convergence of the ground-state energy of H_2O against iteration for $N = 12$.

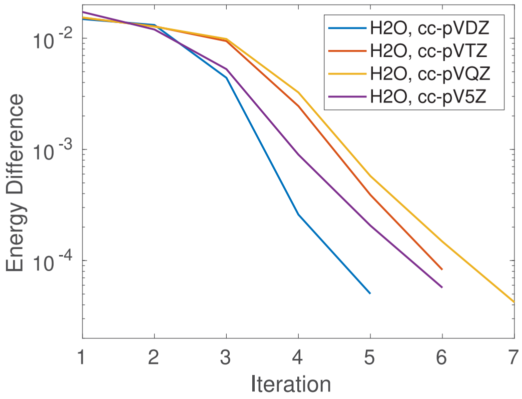

Figure 2. Difference of the ground-state energy of H_2O against iteration for $N = 12$.

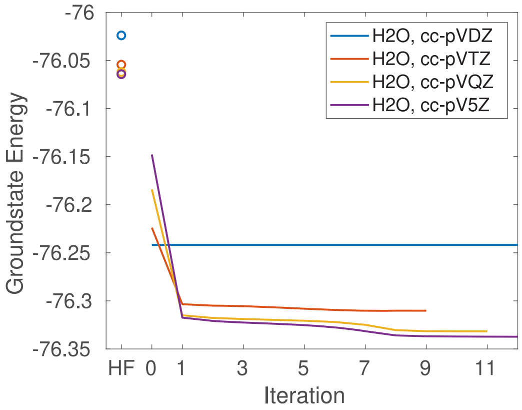

Figure 3. Convergence of the ground-state energy of H_2O against iteration for $N = 24$.

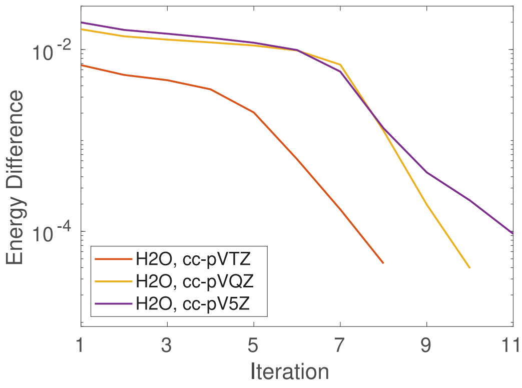

Figure 4. Difference of the ground-state energy of H_2O against iteration for $N = 24$.

Table 2. Ground-State Energies for H_2O with Different Numbers of Selected Orbitals under Variant Basis Sets

	$N = 12$	$N = 24$
basis	GS energy	GS energy
cc-pVDZ	−76.1846948	−76.2418601
cc-pVTZ	−76.2251082	−76.3102225
cc-pVQZ	−76.2352354	−76.3317350
cc-pV5Z	−76.2382165	−76.3372849

In both Figure 1 and Figure 3, we notice that all FCI ground-state energies are lower than the HF energy under any of these basis set. For the first FCI calculation with selected orbitals according to the lowest orbital energies, i.e., iteration 0, we observe that the smaller the basis set the lower the energy. This is likely due to the energy concentration of the orbitals, which means that the smaller basis set has a better concentration of energies among occupied orbitals. As long as an optimized partial unitary matrix U is applied, such an order is no longer preserved starting from iteration 1. In both cases, we also notice that the ordering of energies for different basis sets is revealed after the first two iterations. Starting from then, larger basis sets consistently have lower ground-state energies than the smaller basis sets. The differences between the ground-state energies for different basis sets are much larger than the desired chemical accuracy. Further, in Figure 2 and Figure 4, steady convergence is observed for all experiments and OptOrbFCI converges to a chemical accuracy level within a few iterations. Larger N leads to slightly more iterations in OptOrbFCI.

In addition to Figure 1 and Figure 3, Table 2 further illustrates ground-state energies for both $N = 12$ and $N = 24$. The difference between neighbor basis sets is decreasing as the basis set size increases. The decreases of energies from cc-pVQZ to cc-pV5Z for both N are on the level of millihartree. Hence, the basis limit is nearly achieved for H_2O given $N = 12$ and $N = 24$.

The decrease of the energy as N increases from 12 to 24 is still significant for all basis sets. Hence, we further investigate the relationship between the ground-state energy and the number of selected orbitals, N. Figure 5 shows such a relationship under cc-pVDZ and cc-pVQZ basis sets. As shown in Figure 5, as we gradually increase the number of selected orbitals, the ground-state energy of the cc-pVDZ basis set first decays rapidly for N between 12 and 15, and then, for $N \geq 15$, the decay is much slower. The decay of the ground-state energy of the cc-pVQZ basis set decreased steadily for all N tested here. Hence we expect the slow decay for the cc-pVQZ basis set comes later than $N = 24$, while, under a limited computational budget, the ground-state energy for cc-pVQZ with 24 selected orbitals is already much lower than that of cc-pVDZ with 24 selected orbitals.

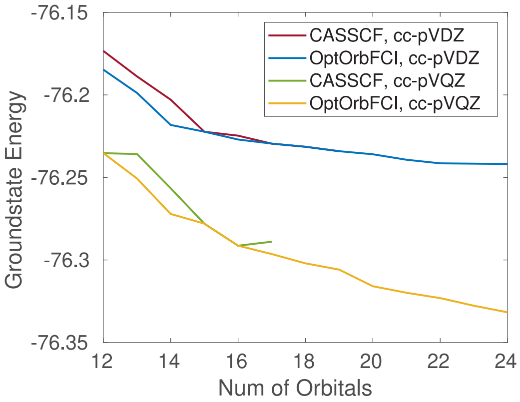

Figure 5. Convergence of the ground-state energy of H_2O against varying N.

In addition to Figure 5, the comparison between OptOrbFCI and CASSCF is detailed in Table 3 and Table 4 for the cc-pVDZ and cc-pVQZ basis sets, respectively. In both tables, we highlight the rows with significantly different ground-state energies. In all cases, OptOrbFCI achieves a lower energy. Since the original optimization problem (eq 14) is nonconvex, any method could be trapped in local minima especially for methods concerning local optimization. OptOrbFCI, using additive random perturbation to initializations in orbital optimization, in many cases avoids the local minima near the initial point. Hence we observe that OptOrbFCI in many cases achieves lower ground-state energy and in no case achieves higher ground-state energy. Here both methods use the same default initial one- and two-body integrals with respect to Hartree-Fock orbitals. When different initializations are considered, the results in Table 3 and Table 4 could be different, while OptOrbFCI is still expected to achieve energies lower than or equal to that of CASSCF. If we further compare the macro iteration numbers, when both methods converge to the same ground-state energy, OptOrbFCI has fewer or an equal number of macro iterations comparing to CASSCF. Even for those cases where the lower ground-state energy is achieved by OptOrbFCI, the difference in the macro iteration numbers is, in most cases, not significant. Hence we conclude that OptOrbFCI could achieve lower ground-state energy and reduce the macro iteration number.

Table 3. Comparison of OptOrbFCI and CASSCF[57] for H_2O under the cc-pVDZ Basis Set[a]

	OptOrbFCI		CASSCF	
Orbs	GS energy	Iter	GS energy	Iter
12	*−76.1847*	*6*	*−76.1734*	*7*
13	*−76.1988*	*8*	*−76.1888*	*7*
14	*−76.2182*	*8*	*−76.2029*	*7*
15	−76.2223	7	−76.2223	7
16	*−76.2270*	*10*	*−76.2247*	*7*
17	−76.2295	6	−76.2295	7
18	−76.2314	6	−76.2314	6
19	−76.2341	3	−76.2341	5
20	−76.2360	3	−76.2360	4

[a] Italic rows indicate significantly different ground-state energies for different methods. Orbs is the number of selected orbitals, and Iter is the macro iteration number.

Table 4. Comparison of OptOrbFCI and CASSCF[57] for H_2O under the cc-pVQZ Basis Set

	OptOrbFCI		CASSCF	
Orbs	GS energy	Iter	GS energy	Iter
12	−76.2352	8	−76.2353	19
13	*−76.2506*	*7*	*−76.2358*	*6*
14	*−76.2721*	*9*	*−76.2566*	*6*
15	−76.2780	5	−76.2780	6
16	−76.2913	15	−76.2914	19
17	*−76.2964*	*18*	*−76.2889*	*8*

4.2. C_2 and N_2.

This section studies OptOrbFCI applied to C_2 and N_2 under their equilibrium geometry; i.e., the bond length for C_2 is 1.24253 Å[12,14] and the bond length for N_2 is 2.118 a_0.[14,58]

The hyper parameters in OptOrbFCI are the same for C_2 and N_2. In CDFCI, the compression threshold is 5×10^{-6}, the tolerance for convergence is 10^{-5}, and the maximum number of iterations is 3×10^7. In the projection method, the convergence tolerance is 10^{-7} and the maximum number of iterations is 10^4. In OptOrbFCI, the convergence tolerance is 10^{-4} and the maximum number of iterations is 20.

Table 5 and Table 6, for C_2 and N_2, respectively, show the properties of the dimers and our numerical results. Since OptOrbFCI selects the number of orbitals the same as that under the cc-pVDZ basis set, the ground-state energies of the cc-

Table 5. Basis Sets and Numerical Results for C_2

molecule	basis	electrons	orbitals	HF energy	selected orbitals	iteration number	OptOrbFCI GS energy
C_2	cc-pVDZ	12	28	−75.4168820	28	-	−75.7319604
	cc-pVTZ	12	60	−75.4014464	28	6	−75.7763001
	cc-pVQZ	12	110	−75.4057650	28	10	−75.7991578
	cc-pV5Z	12	182	−75.4065236	28	12	−75.8030425

Table 6. Basis Sets and Numerical Results for N_2

molecule	basis	electrons	orbitals	HF energy	selected orbitals	iteration number	OptOrbFCI GS energy
N_2	cc-pVDZ	14	28	−108.9493779	28	-	−109.2821727
	cc-pVTZ	14	60	−108.9775136	28	7	−109.3409252
	cc-pVQZ	14	110	−108.9849510	28	7	−109.3639435
	cc-pV5Z	14	182	−108.9866093	28	13	−109.3689430

pVDZ basis set are the FCI results and are used as a reference for the rest results. Similar figures as in the case of H_2O can also be plotted for C_2 and N_2. Since there is not much difference, we omit them from the paper.

Both Table 5 and Table 6 show similar properties, and we discuss their numerical results together. First of all, we notice that any FCI ground-state energy is lower than all the HF energies, which shows that the improvement of the FCI calculation over the HF calculation is beyond the difference between basis sets. Since we fix the number of selected orbitals to the same as that under the cc-pVDZ basis set, the computational cost of the optimal orbital selection method for other basis sets remains the same order as the cost of FCI under the cc-pVDZ basis set. If only the ground-state energy is needed, then OptOrbFCI is roughly twice the iteration number more expensive then that of the FCI under cc-pVDZ. If both the ground-state energy and the RDMs are needed for downstream tasks, then the increasing factor is reduced to the iteration number, which is between 6 and 13. In these estimations, the computational cost of the projection method is ignored. This is the case for the cc-pVTZ and cc-pVQZ basis sets, while for the cc-pV5Z basis set, the computational cost of the projection method is still smaller than that of the CDFCI part but of the same order. Now we provide a few numbers to support this. All the numerical results in this section are performed on a machine with Intel Xeon CPU E5-2687W v3 at 3.10 GHz and 500 GB memory. At least 6 tasks are performed simultaneously. The memory for each problem is limited to 40 GB. Given N selected orbitals, for all basis sets, each CDFCI part (FCI solver plus RDM calculations) costs varying from 10 000 to 50 000 s for C_2, while the computational costs for the projection method parts are dramatically different for different basis sets. The projection method part costs nearly 200 s, 3000 s, and 10 000 s for the cc-pVTZ, cc-pVQZ, and cc-pV5Z basis sets, respectively. The runtime for N_2 has a similar ratio between the CDFCI part and the projection method.

Comparing the ground-state energies under different basis sets, we notice that the lower ground-state energy is achieved under the larger basis set. The improvement between consecutive basis sets, however, is gradually decreasing, close to exponential decay. For both C_2 and N_2, the improvement between the cc-pV5Z and cc-pVQZ basis sets is on the level of millihartree.

4.3. N_2 Binding Curve. This section benchmarks the binding curve of N_2 under the cc-pVQZ basis set with $N = 28$, which is the number of orbitals under the cc-pVDZ basis set. The all-electron N_2 binding curve is well-known to be a difficult problem due to the multireference property for geometry away from equilibrium. In Wang et al.,[14] the binding curve on a very fine grid is produced under the cc-pVDZ basis set up to 10^{-3} mHa accuracy. Here we rebenchmark the binding curve under the cc-pVQZ basis set with $N = 28$ selected orbitals with an accuracy up to 10^{-1} mHa. Since the number of orbitals remains the same, the computational cost of our optimal orbital selection is of the same order as a single CDFCI execution.[14]

For the binding curve, exact same geometries as in Wang et al.[14] are produced. The compression threshold, for the CDFCI part, is 5×10^{-6}, the tolerance for convergence is 10^{-5}, and the maximum number of iterations is 3×10^7. The convergence tolerance for the projection method is 10^{-7}, and the maximum number of iterations is 10^4. For OptOrbFCI, the convergence tolerance is 10^{-4}, and the maximum number of iterations is 20.

Figure 6 illustrates the binding curves of N_2 calculated from CDFCI under the cc-pVDZ basis set[14] and from OptOrbFCI under the cc-pVQZ basis set with $N = 28$. From the figure, in all geometries, OptOrbFCI provides lower variational ground-state energies, while the overall shapes for two curves remain similar. Figure 7 further shows the energy difference of two binding curves, i.e., the ground-state energy of CDFCI minus that of OptOrbFCI. We observe that the decrease is more dramatic when two atoms are closer. There are two nonsmooth points in the energy difference around 2.45 a_0 and 3.2 a_0. Numerically, we also find that the computation is more difficult around these two bond lengths, i.e., the number of iterations increases. Further investigation is needed around these two points.

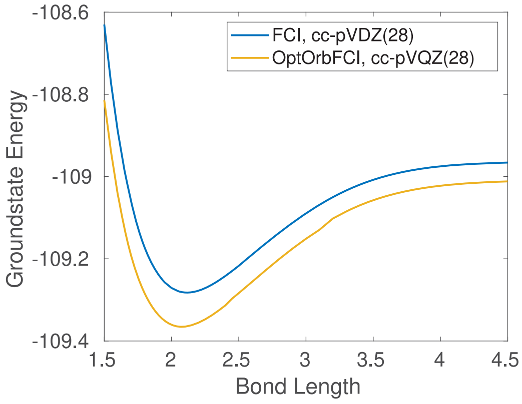

Figure 6. Binding curves for N_2. The blue curve is cited from CDFCI.[14] For each bond length, OptOrbFCI selects 28 orbitals under the cc-pVQZ basis set.

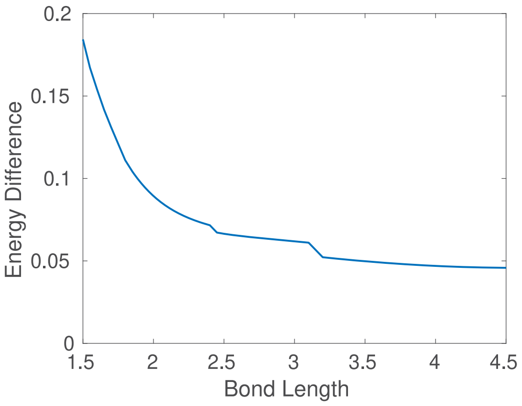

Figure 7. Difference of binding curves for N_2 using FCI under the cc-PVDZ basis set and OptOrbFCI under the cc-pVQZ basis set with $N = 28$.

Comparing to the single ground-state energy, the energy gap is of more chemical relevance. Here, we also include the dissociation energies for N_2 under three settings. The dissociation energy is defined as the difference of ground-state energies at equilibrium geometry (2.118 a_0) and at well separated geometry (4.5 a_0). The three settings are FCI under cc-pVDZ, FCI under cc-pVQZ, and OptOrbFCI under cc-pVQZ with $N = 28$. Numerical results are listed in Table 7. Using the dissociation energy of FCI under cc-pVQZ as a reference solution, we notice that the dissociation energy of OptOrbFCI is more accurate than that of FCI under cc-pVDZ. The error for FCI under cc-pVDZ is about 4×10^{-2} Ha whereas the error for OptOrbFCI is about 10^{-3}, which is on the level of chemical accuracy. Hence we conclude that OptOrbFCI, in addition to providing lower ground-state energies, provides a more accurate dissociation energy.

5. CONCLUSION AND DISCUSSION

We consider the question in this paper for full configuration interaction (FCI) pursuing the basis set limit under a computational budget. We propose a coupled optimization problem (eq 14) as a solution to the question, which is also the formula for CASSCF. The coupling therein between the ground-state wave function $|\Phi\rangle$ and the partial unitary matrix U is complicated. Due to the complication, the optimization problem (eq 14) is then split into two subproblems, eqs 16 and 18, where the former is a standard FCI problem under compressed orbitals and the latter is an optimization of a 4th order polynomial of U with orthonormality constraint. An overall alternating iterative algorithm is proposed to address the optimization problem (eq 14) with the first subproblem (eq 16) solved by a wave function based FCI solver, namely, CDFCI,[14] and the second subproblem (eq 18) solved by a projection method.[46] The overall method above is referred as OptOrbFCI. The method in general is efficient and stable. OptOrbFCI usually converges in 5 to 15 iterations to achieve up to 10^{-1} mHa accuracy. The computational cost, hence, is bounded by that of a few executions of the FCI solver on the selected orbital sets.

Numerically, we apply OptOrbFCI to the water molecule, carbon dimer, and nitrogen dimer under variant basis sets. Under the number of orbitals using the cc-pVDZ basis set, we pursue the FCI calculation under the cc-pVTZ, cc-pVQZ, and cc-pV5Z basis sets. In all cases, we obtain ground-state energies lower than that under cc-pVDZ, where the decrease is beyond chemical accuracy. In the comparison against the conventional CASSCF method,[57] OptOrbFCI could achieve lower ground-state energy and reduce the macro iteration number. The N_2 binding curve is rebenchmarked using OptOrbFCI under the cc-pVQZ basis set with 28 selected orbitals. And the dissociation energy in this case is more accurate than that obtained by the FCI solver under the cc-pVDZ basis set. Hence we conclude that OptOrbFCI coupling with existing FCI solvers is able to pursue the basis set limit under a computational budget.

There are a list of immediate future works of OptOrbFCI. In the current implementation, the orbital symmetry in the given large orbital set is totally ignored; so is the frozen core setting. Under the given large orbital set with orbital symmetry, both the one-body and two-body integrals are of sparse structure. As we ignored the symmetry and frozen core setting, the one-body and two-body integrals of the rotated orbitals are then dense tensors. The downstream FCI problem becomes more expensive. Hence one future work is to implement the rotation under an orbital symmetry constraint and frozen core setting to reduce the cost of FCI solvers. When orbital symmetries are preserved, the corresponding ground-state energy will be lower bounded by that of our current algorithm. Further investigation is needed on the trade-off between the accuracy and the computational cost. A parallelization of the projection method becomes important when the basis set gets large, since the computational bottleneck for the projection method lies in the 4-way tensor contraction, which can be realized as a dense matrix−matrix multiplication. Efficient both distributed-memory and shared-memory parallelizations are manageable. Highly efficient GPU acceleration can also be expected. Besides implementation, further investigation of the convergence property is desired. And extension to low-lying excited states calculation is also a promising future work to be explored. When both ground-state and low-lying excited states are considered under the OptOrbFCI framework with a modified objective function, we expect that the optimal rotation matrix would balance the error among states under consideration and hence potentially provide more accurate approximation to excitation energies than our current algorithm.

■ APPENDIX A: EQUIVALENCE BETWEEN EQUATIONS 10 AND 14

This section provides detailed derivations for the equivalence between eqs 10 and 14. The key step is to show that eq 13 holds for any wave function $|\Phi\rangle$ in $\mathcal{D}[(\psi_1, ..., \psi_M)U] =$

Table 7. Dissociation Energy for N_2

method	basis	electrons	orbitals	GS energy 2.118 a_0	GS energy 4.5 a_0	dissociation energy
FCI[a]	cc-pVDZ	14	28	−109.2821727	−108.9659102	0.3162625
	cc-pVQZ	14	110	−109.4590412	−109.1059938	0.3530474
OptOrbFCI	cc-pVQZ	14	28	−109.3639435	−109.0117220	0.3522214

[a] FCI results are calculated through CDFCI.

https://dx.doi.org/10.1021/acs.jctc.0c00613
J. Chem. Theory Comput. 2020, 16, 6207−6221

$\mathcal{D}[(\phi_1, ..., \phi_N)]$. Since the operators are linear operators and the space is a linear space, it is sufficient to show that eq 13 holds for all bases in $\mathcal{D}[(\phi_1, ..., \phi_N)]$, i.e., all Slater determinants. Any Slater determinant $|D_i\rangle$ in $\mathcal{D}[(\phi_1, ..., \phi_N)]$ can be written as

$$|D_i\rangle = \hat{\boldsymbol{d}}_{i_1}^\dagger \cdots \hat{\boldsymbol{d}}_{i_{n_e}}^\dagger |0\rangle \tag{35}$$

where i_1, ..., i_{n_e} are the index of n_e occupied orbitals and $|0\rangle$ denotes the vacuum state. Now we evaluate the difference of acting $\hat{\boldsymbol{c}}_q$ and $\tilde{\boldsymbol{c}}_q$ on such a Slater determinant. Using the anticommutation relations 11 and 12, the difference can be simplified as

$$\begin{aligned}(\hat{\boldsymbol{c}}_q - \tilde{\boldsymbol{c}}_q)|D_i\rangle &= (\hat{\boldsymbol{c}}_q - \tilde{\boldsymbol{c}}_q)\hat{\boldsymbol{d}}_{i_1}^\dagger \cdots \hat{\boldsymbol{d}}_{i_{n_e}}^\dagger |0\rangle \\ &= (\{\hat{\boldsymbol{c}}_q, \hat{\boldsymbol{d}}_{i_1}^\dagger\} - \{\tilde{\boldsymbol{c}}_q, \hat{\boldsymbol{d}}_{i_1}^\dagger\})\hat{\boldsymbol{d}}_{i_2}^\dagger \cdots \hat{\boldsymbol{d}}_{i_{n_e}}^\dagger |0\rangle \\ &\quad - \hat{\boldsymbol{d}}_{i_1}^\dagger(\hat{\boldsymbol{c}}_q - \tilde{\boldsymbol{c}}_q)\hat{\boldsymbol{d}}_{i_2}^\dagger \cdots \hat{\boldsymbol{d}}_{i_{n_e}}^\dagger |0\rangle \\ &= -\hat{\boldsymbol{d}}_{i_1}^\dagger(\hat{\boldsymbol{c}}_q - \tilde{\boldsymbol{c}}_q)\hat{\boldsymbol{d}}_{i_2}^\dagger \cdots \hat{\boldsymbol{d}}_{i_{n_e}}^\dagger |0\rangle \\ &= (-1)^k \hat{\boldsymbol{d}}_{i_1}^\dagger \cdots \hat{\boldsymbol{d}}_{i_k}^\dagger(\hat{\boldsymbol{c}}_q - \tilde{\boldsymbol{c}}_q)\hat{\boldsymbol{d}}_{i_{k+1}}^\dagger \cdots \hat{\boldsymbol{d}}_{i_{n_e}}^\dagger |0\rangle \\ &= (-1)^{n_e} \hat{\boldsymbol{d}}_{i_1}^\dagger \cdots \hat{\boldsymbol{d}}_{i_{n_e}}^\dagger(\hat{\boldsymbol{c}}_q - \tilde{\boldsymbol{c}}_q)|0\rangle \\ &= 0\end{aligned} \tag{36}$$

where the last equality holds since the annihilation operators acting on the vacuum state vanish. Since any wave function $|\Phi\rangle \in \mathcal{D}[(\phi_1, ..., \phi_N)]$ can be expressed as a linear combination of Slater determinants, i.e., $|\Phi\rangle = \sum_i x_i |D_i\rangle$, where x_i are coefficients, acting the difference of $\hat{\boldsymbol{c}}_q$ and $\tilde{\boldsymbol{c}}_q$ on it leads to

$$(\hat{\boldsymbol{c}}_q - \tilde{\boldsymbol{c}}_q)|\Phi\rangle = \sum_i x_i(\hat{\boldsymbol{c}}_q - \tilde{\boldsymbol{c}}_q)|D_i\rangle = 0 \tag{37}$$

Hence we showed that eq 13 holds for all $|\Phi\rangle \in \mathcal{D}[(\phi_1, ..., \phi_N)]$. The conjugate of eq 13 gives

$$\langle\Phi|\hat{\boldsymbol{c}}_p^\dagger = \langle\Phi|\tilde{\boldsymbol{c}}_p^\dagger \tag{38}$$

The one-body part in the objective function in eq 10 then admits

$$\begin{aligned}&\left\langle \Phi \middle| \sum_{p,q=1}^{M} h_{pq}\hat{\boldsymbol{c}}_p^\dagger\hat{\boldsymbol{c}}_q \middle| \Phi \right\rangle \\ &= \sum_{p,q=1}^{M} h_{pq}\langle\Phi|\tilde{\boldsymbol{c}}_p^\dagger\tilde{\boldsymbol{c}}_q|\Phi\rangle \\ &= \sum_{p,q=1}^{M} h_{pq} \sum_{p',q'=1}^{N} \langle\Phi|\hat{\boldsymbol{d}}_{p'}^\dagger\hat{\boldsymbol{d}}_{q'}|\Phi\rangle U_{pp'}U_{qq'} \\ &= \left\langle \Phi \middle| \sum_{p',q'=1}^{N} \tilde{h}_{p'q'}\hat{\boldsymbol{d}}_{p'}^\dagger\hat{\boldsymbol{d}}_{q'} \middle| \Phi \right\rangle\end{aligned} \tag{39}$$

where $\tilde{h}_{p'q'}$ is defined as eq 7. The one-body part in the objective function in eq 10, hence, is equivalent to that in eq 14.

In order to show the equivalence of the two-body part in both objective functions, we need two more anticommutation relations. The anticommutation relation between $\hat{\boldsymbol{c}}_s$ and $\tilde{\boldsymbol{c}}_r$ satisfies

$$\begin{aligned}\{\hat{\boldsymbol{c}}_s, \tilde{\boldsymbol{c}}_r\} &= \left\{\hat{\boldsymbol{c}}_s, \sum_{r'=1}^{N} \hat{\boldsymbol{d}}_{r'}U_{rr'}\right\} \\ &= \sum_{r'=1}^{N}\sum_{r''=1}^{M} \{\hat{\boldsymbol{c}}_s, \hat{\boldsymbol{c}}_{r''}\}U_{rr'}U_{r''r'} \\ &= 0\end{aligned} \tag{40}$$

Similarly, we also have the anticommutation relation between $\tilde{\boldsymbol{c}}_p^\dagger$ and $\hat{\boldsymbol{c}}_q^\dagger$,

$$\{\tilde{\boldsymbol{c}}_p^\dagger, \hat{\boldsymbol{c}}_q^\dagger\} = 0 \tag{41}$$

The anticommutation relations within $\tilde{\boldsymbol{c}}$s can also be derived in an analog way. The two-body part in the objective function in eq 10 then admits

$$\begin{aligned}\left\langle \Phi \middle| \sum_{p,q,r,s=1}^{M} v_{pqrs}\hat{\boldsymbol{c}}_p^\dagger\hat{\boldsymbol{c}}_q^\dagger\hat{\boldsymbol{c}}_s\hat{\boldsymbol{c}}_r \middle| \Phi \right\rangle &= \sum_{p,q,r,s=1}^{M} v_{pqrs}\langle\Phi|\tilde{\boldsymbol{c}}_p^\dagger\hat{\boldsymbol{c}}_q^\dagger\hat{\boldsymbol{c}}_s\tilde{\boldsymbol{c}}_r|\Phi\rangle \\ &= \sum_{p,q,r,s=1}^{M} v_{pqrs}\langle\Phi|\hat{\boldsymbol{c}}_q^\dagger\tilde{\boldsymbol{c}}_p^\dagger\tilde{\boldsymbol{c}}_r\hat{\boldsymbol{c}}_s|\Phi\rangle \\ &= \sum_{p,q,r,s=1}^{M} v_{pqrs}\langle\Phi|\tilde{\boldsymbol{c}}_p^\dagger\tilde{\boldsymbol{c}}_q^\dagger\tilde{\boldsymbol{c}}_s\tilde{\boldsymbol{c}}_r|\Phi\rangle \\ &= \sum_{p',q',r',s'=1}^{N}\sum_{p,q,r,s=1}^{M} v_{pqrs}U_{pp'}U_{qq'}U_{rr'}U_{ss'} \\ &\quad \cdot\langle\Phi|\hat{\boldsymbol{d}}_{p'}^\dagger\hat{\boldsymbol{d}}_{q'}^\dagger\hat{\boldsymbol{d}}_{s'}\hat{\boldsymbol{d}}_{r'}|\Phi\rangle \\ &= \left\langle \Phi \middle| \sum_{p',q',r',s'=1}^{M} \tilde{v}_{p'q'r's'}\hat{\boldsymbol{d}}_{p'}^\dagger\hat{\boldsymbol{d}}_{q'}^\dagger\hat{\boldsymbol{d}}_{s'}\hat{\boldsymbol{d}}_{r'} \middle| \Phi \right\rangle\end{aligned} \tag{42}$$

where the second equality applies the anticommutation relations in eqs 40 and 41, the third equality applies the anticommutation relations within $\tilde{\boldsymbol{c}}$s, and $\tilde{v}_{p'q'r's'}$ is defined as eq 8. The two-body part in the objective function in eq 10, hence, is equivalent to that in eq 14.

Combining eqs 39 and 42, we conclude that the objective functions in eqs 10 and 14 are equivalent given the wave function $|\Phi\rangle \in \mathcal{D}[(\phi_1, ..., \phi_N)]$.

Table 8. Ground-State Energies for N_2 with Bond Lengths Smaller than 2.118 a_0

	FCI	OptOrb
bond length (a_0)	cc-pVDZ (Ha)	cc-pVQZ(28) (Ha)
1.500	−108.6300476	−108.8144031
1.550	−108.7719968	−108.9391824
1.600	−108.8888460	−109.0429050
1.650	−108.9843136	−109.1260152
1.700	−109.0615754	−109.1926550
1.750	−109.1233484	−109.2443696
1.800	−109.1719641	−109.2830113
1.850	−109.2094264	−109.3137005
1.900	−109.2374578	−109.3359754
1.950	−109.2575411	−109.3511562
2.000	−109.2709530	−109.3603603
2.050	−109.2787896	−109.3645818
2.100	−109.2819938	−109.3647561
2.118	−109.2821727	−109.3639435

Table 9. Ground-State Energies for N_2 with Bond Lengths Larger than 2.118 a_0

	FCI	OptOrb
bond length (a_0)	cc-pVDZ (Ha)	cc-pVQZ(28) (Ha)
2.118	−109.2821727	−109.3639435
2.150	−109.2813737	−109.3614955
2.200	−109.2776211	−109.3555534
2.250	−109.2713283	−109.3473397
2.300	−109.2630013	−109.3373910
2.350	−109.2530718	−109.3259793
2.400	−109.2419079	−109.3135325
2.450	−109.2298228	−109.2970156
2.500	−109.2170830	−109.2835331
2.600	−109.1905077	−109.2557994
2.700	−109.1635998	−109.2279395
2.800	−109.1373583	−109.2008712
2.900	−109.1124729	−109.1751472
3.000	−109.0894053	−109.1512795
3.100	−109.0684502	−109.1295149
3.200	−109.0497787	−109.1020069
3.300	−109.0334619	−109.0848174
3.400	−109.0194835	−109.0700669
3.500	−109.0077466	−109.0575569
3.600	−108.9980829	−109.0471986
3.700	−108.9902691	−109.0387653
3.800	−108.9840499	−109.0319008
3.900	−108.9791625	−109.0265483
4.000	−108.9753572	−109.0223481
4.100	−108.9724102	−109.0189859
4.200	−108.9701316	−109.0164481
4.300	−108.9683664	−109.0144948
4.400	−108.9669909	−109.0129196
4.500	−108.9659102	−109.0117220

APPENDIX B: N_2 BINDING CURVE

The N_2 binding curve is plotted in Figure 6, and the detailed energies are given in Table 8 and Table 9. Table 8 provides the ground-state energies for N_2 with bond length smaller than that at equilibrium geometry, whereas Table 9 provides the ground-state energies with bond length greater than that at equilibrium geometry. In both tables, we apply OptOrbFCI to compute the ground-state energies of N_2 under the cc-pVQZ basis set with 28 selected orbitals. The same list of bond lengths as that in Wang et al.[14] is adopted here. The ground-state energies of FCI under the cc-pVDZ basis set are cited from Wang et al.[14]

AUTHOR INFORMATION

Corresponding Authors

Yingzhou Li − *Department of Mathematics, Duke University, Durham, North Carolina 27708, United States;* orcid.org/0000-0003-1852-3750; Email: yingzhou.li@duke.edu

Jianfeng Lu − *Department of Mathematics and Department of Chemistry and Department of Physics, Duke University, Durham, North Carolina 27708, United States;* Email: jianfeng@math.duke.edu

Complete contact information is available at:
https://pubs.acs.org/10.1021/acs.jctc.0c00613

Funding

The work is supported in part by the U.S. National Science Foundation under Awards DMS-1454939 and DMS-2012286 and by the U.S. Department of Energy via Grant DE-SC0019449.

Notes

The authors declare no competing financial interest.

ACKNOWLEDGMENTS

The authors thank Zhe Wang for helpful discussions. The authors also thank Jonathon Misiewicz and Qiming Sun for constructive suggestions on the comparison with CASSCF.

REFERENCES

(1) Chan, G. K.-L.; Sharma, S. The density matrix renormalization group in quantum chemistry. *Annu. Rev. Phys. Chem.* **2011**, *62*, 465−481.

(2) Olivares-Amaya, R.; Hu, W.; Nakatani, N.; Sharma, S.; Yang, J.; Chan, G. K.-L. The ab-initio density matrix renormalization group in practice. *J. Chem. Phys.* **2015**, *142*, 034102.

(3) Booth, G. H.; Thom, A. J. W.; Alavi, A. Fermion Monte Carlo without fixed nodes: A game of life, death, and annihilation in Slater determinant space. *J. Chem. Phys.* **2009**, *131*, 054106.

(4) Booth, G. H.; Grüneis, A.; Kresse, G.; Alavi, A. Towards an exact description of electronic wavefunctions in real solids. *Nature* **2013**, *493*, 365−370.

(5) Cleland, D.; Booth, G. H.; Alavi, A. Communications: Survival of the fittest: Accelerating convergence in full configuration-interaction quantum Monte Carlo. *J. Chem. Phys.* **2010**, *132*, 041103.

(6) Petruzielo, F. R.; Holmes, A. A.; Changlani, H. J.; Nightingale, M. P.; Umrigar, C. J. Semistochastic projector Monte Carlo method. *Phys. Rev. Lett.* **2012**, *109*, 230201.

(7) Lu, J.; Wang, Z. The full configuration interaction quantum Monte Carlo method in the lens of inexact power iteration. *SIAM J. Sci. Comput.* **2020**, *42*, B1−B29.

(8) Huron, B.; Malrieu, J. P.; Rancurel, P. Iterative perturbation calculations of ground and excited state energies from multiconfigurational zeroth-order wavefunctions. *J. Chem. Phys.* **1973**, *58*, 5745−5759.

(9) Schriber, J. B.; Evangelista, F. A. Communication: An adaptive configuration interaction approach for strongly correlated electrons with tunable accuracy. *J. Chem. Phys.* **2016**, *144*, 161106.

(10) Tubman, N. M.; Lee, J.; Takeshita, T. Y.; Head-Gordon, M.; Whaley, K. B. A deterministic alternative to the full configuration interaction quantum Monte Carlo method. *J. Chem. Phys.* **2016**, *145*, 044112.

(11) Tubman, N. M.; Freeman, C. D.; Levine, D. S.; Hait, D.; Head-Gordon, M.; Whaley, K. B. Modern approaches to exact diagonalization and selected configuration interaction with the adaptive sampling CI method. *arXiv*, 2018; http://arxiv.org/abs/1807.00821.

(12) Holmes, A. A.; Tubman, N. M.; Umrigar, C. J. Heat-bath configuration interaction: An efficient selected configuration interaction algorithm inspired by heat-bath sampling. *J. Chem. Theory Comput.* **2016**, *12*, 3674−3680.

(13) Sharma, S.; Holmes, A. A.; Jeanmairet, G.; Alavi, A.; Umrigar, C. J. Semistochastic heat-bath configuration interaction method: Selected configuration interaction with semistochastic perturbation theory. *J. Chem. Theory Comput.* **2017**, *13*, 1595−1604.

(14) Wang, Z.; Li, Y.; Lu, J. Coordinate descent full configuration interaction. *J. Chem. Theory Comput.* **2019**, *15*, 3558−3569.

(15) Greene, S. M.; Webber, R. J.; Weare, J.; Berkelbach, T. C. Beyond walkers in stochastic quantum chemistry: Reducing error using fast randomized iteration. *arXiv*, 2019; http://arxiv.org/abs/1905.00995.

(16) Lim, L.-H.; Weare, J. Fast randomized iteration: Diffusion Monte Carlo through the lens of numerical linear algebra. *SIAM Rev.* **2017**, *59*, 547−587.

(17) Li, Y.; Lu, J.; Wang, Z. Coordinatewise descent methods for leading eigenvalue problem. *SIAM J. Sci. Comput.* **2019**, *41*, A2681−A2716.

(18) Hernandez, T. M.; Van Beeumen, R.; Caprio, M. A.; Yang, C. A greedy algorithm for computing eigenvalues of a symmetric matrix. *arXiv*, 2019; http://arxiv.org/abs/1911.10041.

(19) Gao, W.; Li, Y.; Lu, B. Triangularized orthogonalization-free method for solving extreme eigenvalue problems. *arXiv*, 2020; http://arxiv.org/abs/2005.12161.

(20) Bytautas, L.; Ivanic, J.; Ruedenberg, K. Split-localized orbitals can yield stronger configuration interaction convergence than natural orbitals. *J. Chem. Phys.* **2003**, *119*, 8217−8224.

(21) Zhang, J. M.; Kollar, M. Optimal multiconfiguration approximation of an *N*-fermion wave function. *Phys. Rev. A: At., Mol., Opt. Phys.* **2014**, *89*, 012504.

(22) Giesbertz, K. J. H. Are natural orbitals useful for generating an efficient expansion of the wave function? *Chem. Phys. Lett.* **2014**, *591*, 220−226.

(23) Alcoba, D. R.; Torre, A.; Lain, L.; Massaccesi, G. E.; Oña, O. B.; Ayers, P. W.; Van Raemdonck, M.; Bultinck, P.; Van Neck, D. Performance of Shannon-entropy compacted *N*-electron wave functions for configuration interaction methods. *Theor. Chem. Acc.* **2016**, *135*, 153.

(24) Kivlichan, I. D.; McClean, J. R.; Wiebe, N.; Gidney, C.; Aspuru-Guzik, A.; Chan, G. K.-L.; Babbush, R. Quantum simulation of electronic structure with linear depth and connectivity. *Phys. Rev. Lett.* **2018**, *120*, 110501.

(25) Babbush, R.; Berry, D. W.; McClean, J. R.; Neven, H. Quantum simulation of chemistry with sublinear scaling in basis size. *npj Quantum Inf.* **2019**, *5*, 92.

(26) Siegbahn, P. E.; Heiberg, A.; Roos, B.; Levy, B. A comparison of the super-Cl and the Newton-Raphson scheme in the complete active space SCF method. *Phys. Scr.* **1980**, *21*, 323−237.

(27) Roos, B. O.; Taylor, P. R.; Sigbahn, P. E. A complete active space SCF method (CASSCF) using a density matrix formulated super-CI approach. *Chem. Phys.* **1980**, *48*, 157−173.

(28) Siegbahn, P. E.; Almlöf, J.; Heiberg, A.; Roos, B. O. The complete active space SCF (CASSCF) method in a Newton-Raphson formulation with application to the HNO molecule. *J. Chem. Phys.* **1981**, *74*, 2384−2396.

(29) Knowles, P. J.; Werner, H. J. An efficient second-order MC SCF method for long configuration expansions. *Chem. Phys. Lett.* **1985**, *115*, 259−267.

(30) Zgid, D.; Nooijen, M. The density matrix renormalization group self-consistent field method: Orbital optimization with the density matrix renormalization group method in the active space. *J. Chem. Phys.* **2008**, *128*, 144116.

(31) Ghosh, D.; Hachmann, J.; Yanai, T.; Chan, G. K.-L. Orbital optimization in the density matrix renormalization group, with applications to polyenes and *β*-carotene. *J. Chem. Phys.* **2008**, *128*, 144117.

(32) Yanai, T.; Kurashige, Y.; Ghosh, D.; Chan, G. K.-L. Accelerating convergence in iterative solution for large-scale complete active space self-consistent-field calculations. *Int. J. Quantum Chem.* **2009**, *109*, 2178−2190.

(33) Olsen, J. The CASSCF method: A perspective and commentary. *Int. J. Quantum Chem.* **2011**, *111*, 3267−3272.

(34) Wouters, S.; Bogaerts, T.; Van der Voort, P.; Van Speybroeck, V.; Van Neck, D. Communication: DMRG-SCF study of the singlet, triplet, and quintet states of oxo-Mn(Salen). *J. Chem. Phys.* **2014**, *140*, 241103.

(35) Li Manni, G.; Smart, S. D.; Alavi, A. Combining the complete active space self-consistent field method and the full configuration interaction quantum Monte Carlo within a super-CI framework, with application to challenging metal-porphyrins. *J. Chem. Theory Comput.* **2016**, *12*, 1245−1258.

(36) Freitag, L.; Knecht, S.; Angeli, C.; Reiher, M. Multireference perturbation theory with Cholesky decomposition for the density matrix renormalization group. *J. Chem. Theory Comput.* **2017**, *13*, 451−459.

(37) Ma, Y.; Knecht, S.; Keller, S.; Reiher, M. Second-order self-consistent-field density-matrix renormalization group. *J. Chem. Theory Comput.* **2017**, *13*, 2533−2549.

(38) Smith, J. E.; Mussard, B.; Holmes, A. A.; Sharma, S. Cheap and near exact CASSCF with large active spaces. *J. Chem. Theory Comput.* **2017**, *13*, 5468−5478.

(39) Sun, Q.; Yang, J.; Chan, G. K. L. A general second order complete active space self-consistent-field solver for large-scale systems. *Chem. Phys. Lett.* **2017**, *683*, 291−299.

(40) Freitag, L.; Ma, Y.; Baiardi, A.; Knecht, S.; Reiher, M. Approximate analytical gradients and nonadiabatic couplings for the state-average density matrix renormalization group self-consistent-field method. *J. Chem. Theory Comput.* **2019**, *15*, 6724−6737.

(41) Kreplin, D. A.; Knowles, P. J.; Werner, H. J. Second-order MCSCF optimization revisited. I. Improved algorithms for fast and robust second-order CASSCF convergence. *J. Chem. Phys.* **2019**, *150*, 194106.

(42) Levine, D. S.; Hait, D.; Tubman, N. M.; Lehtola, S.; Whaley, K. B.; Head-Gordon, M. CASSCF with extremely large active spaces using the adaptive sampling configuration interaction method. *J. Chem. Theory Comput.* **2020**, *16*, 2340.

(43) Ruedenberg, K.; Cheung, L. M.; Elbert, S. T. MCSCF optimization through combined use of natural orbitals and the Brillouin-Levy-Berthier theorem. *Int. J. Quantum Chem.* **1979**, *16*, 1069−1101.

(44) Wen, Z.; Yin, W. A feasible method for optimization with orthogonality constraints. *Math. Program.* **2013**, *142*, 397−434.

(45) Gao, B.; Liu, X.; Yuan, Y.-x. Parallelizable algorithms for optimization problems with orthogonality constraints. *SIAM J. Sci. Comput.* **2019**, *41*, A1949−A1983.

(46) Gao, B.; Liu, X.; Chen, X.; Yuan, Y. X. A new first-order algorithmic framework for optimization problems with orthogonality constraints. *SIAM J. Optim.* **2018**, *28*, 302−332.

(47) Zhang, X.; Zhu, J.; Wen, Z.; Zhou, A. Gradient type optimization methods for electronic structure calculations. *SIAM J. Sci. Comput.* **2014**, *36*, C265−C289.

(48) Huang, W.; Gallivan, K. A.; Absil, P.-A. A Broyden class of quasi-Newton methods for Riemannian optimization. *SIAM J. Optim.* **2015**, *25*, 1660−1685.

(49) Li Manni, G.; Alavi, A. Understanding the mechanism stabilizing intermediate spin states in Fe(II)-porphyrin. *J. Phys. Chem. A* **2018**, *122*, 4935−4947.

(50) Deng, W.; Yin, W. On the global and linear convergence of the generalized alternating direction method of multipliers. *J. Sci. Comput.* **2016**, *66*, 889−916.

(51) Nesterov, Y. Efficiency of coordinate descent methods on huge-scale optimization problems. *SIAM J. Optim.* **2012**, *22*, 341−362.

(52) Wright, S. J. Coordinate descent algorithms. *Math. Program.* **2015**, *151*, 3−34.

(53) Shi, H.-J. M.; Tu, S.; Xu, Y.; Yin, W. A primer on coordinate descent algorithms. *arXiv*, 2016. http://arxiv.org/abs/1610.00040.

(54) Banerjee, A. S.; Grein, F. Convergence behavior of some multiconfiguration methods. *Int. J. Quantum Chem.* **1976**, *10*, 123−134.

(55) Parrish, R. M.; Burns, L. A.; Smith, D. G. A.; Simmonett, A. C.; DePrince, A. E.; Hohenstein, E. G.; Bozkaya, U.; Sokolov, A. Y.; Di Remigio, R.; Richard, R. M.; Gonthier, J. F.; James, A. M.; McAlexander, H. R.; Kumar, A.; Saitow, M.; Wang, X.; Pritchard, B. P.; Verma, P.; Schaefer, H. F.; Patkowski, K.; King, R. A.; Valeev, E. F.; Evangelista, F. A.; Turney, J. M.; Crawford, T. D.; Sherrill, C. D. Psi4 1.1: An open-source electronic structure program emphasizing automation, advanced libraries, and interoperability. *J. Chem. Theory Comput.* **2017**, *13*, 3185−3197.

(56) Wang, Z.; Li, Y.; Lu, J. *CDFCI*. 2020. https://github.com/quantum/CDFCI.

(57) Sun, Q.; Berkelbach, T. C.; Blunt, N. S.; Booth, G. H.; Guo, S.; Li, Z.; Liu, J.; McClain, J. D.; Sayfutyarova, E. R.; Sharma, S.; Wouters, S.; Chan, G. K. *PySCF: the Python-based simulations of chemistry framework*. 2017. https://onlinelibrary.wiley.com/doi/abs/10.1002/wcms.1340.

(58) Chan, G. K. L.; Kállay, M.; Gauss, J. State-of-the-art density matrix renormalization group and coupled cluster theory studies of the nitrogen binding curve. *J. Chem. Phys.* **2004**, *121*, 6110−6116.